Analytica Chimica Acta 1408 (2026) 345572

Contents lists available at ScienceDirect

Analytica Chimica Acta

journal homepage: www.elsevier.com/locate/aca

A self-calibrating dual-channel MOF-based fluorescent sensor for rapid and visual phosphate detection

Jinfeng Zhou [a,*], Hailin Qiu [b], Qing Zhou [c], Chunjie Chu [a], Xiaodong Zhang [a], Yanhong Xu [a]

[a] College of Materials Science and Engineering, Pingdingshan University, Pingdingshan, 467000, PR China
[b] Orient KOJI Limited, Tianjin, 300122, PR China
[c] Fujian Engineering Research Center of Advanced Manufacturing Technology for Fine Chemicals, College of Chemical Engineering, Fuzhou University, Fuzhou, 350116, PR China

HIGHLIGHTS

- A self-calibrating dual-channel fluorescent sensor is constructed based on a MOF platform.
- A phosphate-insensitive internal reference and a Eu^{3+}-responsive channel are spatially integrated.
- Phosphate detection is achieved via competitive coordination-induced ratiometric fluorescence.
- Rapid, visual, and semi-quantitative phosphate detection is enabled with smartphone readout.
- Accurate phosphate analysis in real water samples demonstrates practical applicability.

GRAPHICAL ABSTRACT

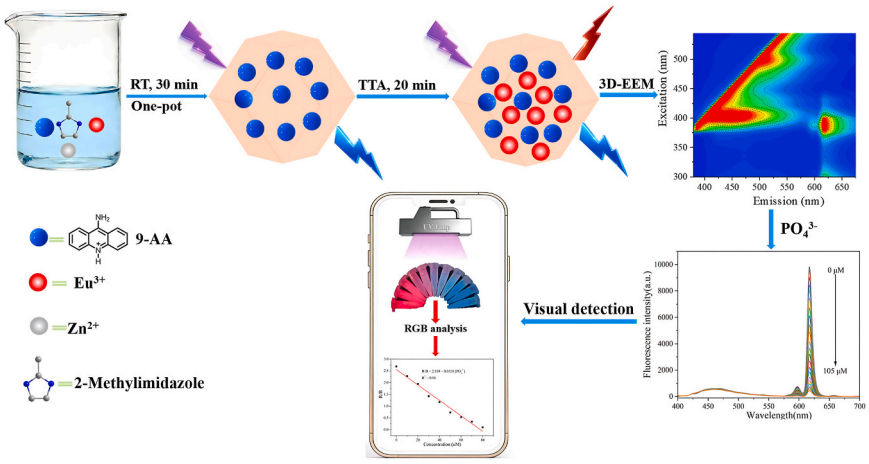

ARTICLE INFO

Handling Editor: Dr. J.P. Landers

Keywords:
Ratiometric fluorescence
Phosphate detection
Visual sensing
Metal–organic frameworks

ABSTRACT

Rapid and reliable phosphate (Pi; PO_4^{3-}) sensing is of critical importance for environmental monitoring, yet remains challenging due to signal instability and limited field deployability of existing methods. Herein, we report a self-calibrating dual-channel fluorescent sensor based on a metal-organic framework (MOF), denoted as 9-AA@Eu-ZIF-8@TTA, for rapid and visual Pi detection. The sensor is rationally constructed through a modular host-guest and coordination assembly strategy, in which a Pi-insensitive blue-emissive dye (acridin-9-amine, 9-AA) is encapsulated within Eu^{3+}-doped ZIF-8 as an internal reference, while a red-emissive Eu^{3+}-TTA coordination complex serves as the responsive channel. Pi detection is governed by a competitive coordination mechanism, where Pi preferentially binds to Eu^{3+}, displacing the antenna ligand TTA and selectively quenching the Eu^{3+}-centered emission at 617 nm without affecting the reference signal. This dual-channel response enables reliable ratiometric quantification of Pi over a linear range of 0–80 μM with a detection limit of 0.48 μM and a rapid response time of 0.5 min. The sensor exhibits excellent stability over a wide pH range (3–11) and high

* Corresponding author.
E-mail address: zhoujf016@163.com (J. Zhou).

https://doi.org/10.1016/j.aca.2026.345572
Received 2 April 2026; Accepted 21 April 2026
Available online 22 April 2026

selectivity against competing ions. Importantly, the distinct red-to-blue fluorescence transition under UV excitation allows direct visual discrimination of Pi levels, while smartphone-based RGB analysis enables instrument-free quantitative readout. Accurate Pi determination in real water samples further demonstrates the practical applicability of this sensor. This work provides a versatile MOF-based design strategy for constructing robust ratiometric fluorescent sensors through the integration of host–guest chemistry and analyte-triggered coordination interactions.

1. Introduction

Phosphate (Pi; PO_4^{3-}) plays a dual role as an indispensable nutrient and a potential environmental pollutant, depending on its concentration and distribution [1,2].

In aquatic ecosystems, Pi is a critical nutrient that supports the growth of plants and microorganisms [3]. However, excessive Pi inputs from agricultural runoff and domestic wastewater are a primary cause of eutrophication, leading to harmful algal blooms, oxygen depletion, and severe ecological imbalance [4,5]. In biological systems, Pi is integral to energy metabolism (ATP), nucleic acid synthesis (DNA/RNA), and maintenance of cellular membranes (phospholipid bilayers) [6–8]. However, abnormal Pi levels are closely associated with metabolic disorders and cardiovascular diseases [9–12]. Accordingly, the development of reliable, sensitive, and selective methods for Pi detection is of significant importance for environmental monitoring, clinical diagnostics, and food safety.

A variety of analytical techniques have been developed for Pi determination, including colorimetric assays [13–16], electrochemical methods [17–20], spectrophotometric approaches [2,21,22], and chromatographic techniques [23]. Despite their widespread use, these methods often rely on elaborate sample pretreatment, sophisticated instrumentation, and time-consuming procedures, which limit their applicability in real-time monitoring and field-deployable analysis. Fluorescence-based sensing has therefore emerged as an attractive alternative due to its high sensitivity, rapid response, and operational simplicity [24–26]. Among these strategies, ratiometric fluorescent probes, which employ dual-emission signals for self-calibration, provide improved quantitative accuracy by minimizing the influence of environmental fluctuations and instrumental variations [27–31]. Moreover, the visually distinguishable color changes associated with ratiometric responses enable intuitive signal readout under ultraviolet illumination, rendering such probes highly suitable for portable and on-site sensing platforms. To date, numerous ratiometric fluorescent probes have been reported for Pi detection [3,32–36]. Nevertheless, many existing systems still suffer from intrinsic limitations, including insufficient stability in aqueous media, signal cross-talk between emissive components, complex fabrication procedures, or inadequate selectivity in the presence of competing anions, which restrict their practical applicability in complex samples.

Metal−organic frameworks (MOFs) have attracted increasing attention as fluorescence sensing platforms due to their high porosity, large surface area, and structural tunability [29,37–39]. Compared with conventional small−molecule probes, MOF−based sensors can enrich target analytes, thereby amplifying sensing responses, and have been successfully explored for Pi detection in aqueous environments [3,32–36]. In particular, the strong coordination affinity between Pi and Eu^{3+} ions has been widely exploited to construct Pi-responsive luminescent sensors based on ligand displacement, antenna deactivation, or framework perturbation mechanisms, which collectively originate from the strong Eu-*O*-P coordination interactions [3,36,40–43]. However, in many reported Eu^{3+}-based MOF sensors, Pi binding often induces uncontrolled and nonlocalized perturbation of the Eu^{3+} coordination environment, which may lead to emission crosstalk between multiple emissive components and, in some cases, partial framework degradation [36,41,42]. As a consequence, the stability of the reference signal and the reliability of ratiometric quantification are frequently compromised under practical sensing conditions. Therefore, the rational integration of a Pi-responsive Eu^{3+}-centered emission with a stable and Pi-insensitive internal reference within a single MOF platform−while enabling spatially confined and precisely regulated modulation of the Eu^{3+} coordination environment—remains a critical challenge for the development of robust ratiometric Pi sensors.

Herein, we report a rationally designed dual-channel MOF-based fluorescent sensor that directly addresses the above challenge through a facile and modular assembly strategy, enabling the spatial and functional integration of a stable internal reference and a selectively responsive Eu^{3+}-centered emission within a single framework. The resulting composite, denoted as 9-AA@Eu-ZIF-8@TTA, is constructed via a combination of host–guest encapsulation and coordination assembly. In this system, a blue-emissive dye, acridin-9-amine (9-AA), is physically confined within the pores of Eu^{3+}-doped ZIF-8 and serves as a Pi-insensitive internal reference, while coordination of the antenna ligand 2-thenoyltrifluoroacetone (TTA) to Eu^{3+} centers generates a red-emissive responsive channel. Pi sensing is governed by a competitive coordination mechanism, in which Pi preferentially binds to Eu^{3+} and selectively displace the TTA ligand, resulting in efficient quenching of the Eu^{3+}-centered emission without perturbing the reference signal. This localized and selective modulation produces a pronounced ratiometric fluorescence response (F_{617}/F_{460}), enabling accurate and self-calibrated Pi detection accompanied by a distinct red-to-blue color transition under UV excitation. Furthermore, integration of the ratiometric color response with smartphone-based RGB analysis allows visual signals to be converted into quantitative data, providing a practical route for instrument-free and on-site Pi monitoring. More broadly, this work establishes a general MOF-based design strategy for constructing robust ratiometric fluorescent sensors by integrating host−guest chemistry with analyte-triggered coordination interactions.

2. Experimental section

2.1. Materials

All chemicals and reagents were purchased from commercial suppliers and used as received unless otherwise stated. Sodium phosphate (Na_3PO_4, 99.9%) and thenoyltrifluoroacetone (TTA) were purchased from Shanghai Macklin Reagent Co., Ltd, China. Zinc (II) nitrate hexahydrate ($Zn(NO_3)_2{\cdot}6H_2O$, 99%), 2-methylimidazole (99%), acridin-9-amine (9-AA, 99.9%) and europium (III) nitrate hexahydrate ($Eu(NO_3)_3{\cdot}6H_2O$, 99.9%) were obtained from Alfa Aesar Chemical Co., Ltd, China. Sodium phosphite ($Na_2HPO_3{\cdot}2H_2O$, 99%), sodium pyrophosphate ($Na_4P_2O_7$, 99%), trimethyl phosphate (TMP) and dimethyl methylphosphonate (DMMP) were bought from Aladdin Chemistry Co. Ltd. (Shanghai, China). Throughout all experiments, ultrapure water with a resistivity of 18.2 MΩ cm, produced by a Milli-Q water purification system (Millipore), was used. Filter papers were provided by Cytiva Biotechnology (Hangzhou) Co., Ltd.

2.2. Instruments

Powder X-ray diffraction (PXRD) patterns were recorded on a Bruker D8 Advance diffractometer using Cu Kα radiation (λ = 1.5406 Å). Fourier-transform infrared (FT-IR) spectra were collected in the range of 4000–400 cm^{-1} on a Nicolet 380 spectrometer using KBr pellets. UV-vis

absorption measurements were carried out using a PerkinElmer Lambda 950 spectrophotometer. Steady-state fluorescence emission spectra were measured on a Hitachi F-7000 fluorescence spectrophotometer. Time-resolved fluorescence decay measurements were performed by time-correlated single-photon counting (TCSPC) using a Horiba FluoroLog-3 system equipped with a DeltaDiode-365 pulsed laser. The morphology and elemental distribution of the samples were examined by transmission electron microscopy (TEM) and energy-dispersive X-ray spectroscopy (EDS) mapping on an FEI Tecnai G2 F20 microscope. Hydrodynamic particle size distributions were determined by dynamic light scattering (DLS) using a Malvern Zetasizer Nano instrument. X-ray photoelectron spectroscopy (XPS) measurements were carried out on a Thermo Scientific ESCALAB 250Xi spectrometer with monochromated Al Kα radiation.

2.3. Material synthesis

2.3.1. Synthesis of 9-AA@Eu-ZIF-8

2-Methylimidazole (2.0 g, 24.36 mmol) was dissolved in H_2O (8.0 mL). Separately, 9-AA (2.0 mg, 0.015 mmol) was dissolved in methanol (1.0 mL), and $Zn(NO_3)_2{\cdot}6H_2O$ (200 mg, 0.67 mmol) and $Eu(NO_3)_3{\cdot}6H_2O$ (100 mg, 0.22 mmol) were each dissolved in H_2O (2.0 mL). The $Zn(NO_3)_2{\cdot}6H_2O$, $Eu(NO_3)_3{\cdot}6H_2O$, and 9-AA solutions were combined and stirred for 2 min, followed by dropwise addition of the 2-methylimidazole solution. The mixture was then stirred at room temperature for 30 min. The resulting suspension was collected by centrifugation, washed with water and ethanol, and dried to afford 9-AA@Eu-ZIF-8. For comparison, Eu-ZIF-8 was synthesized under identical conditions without 9-AA.

2.3.2. Synthesis of 9-AA@Eu-ZIF-8@TTA

9-AA@Eu-ZIF-8@TTA was prepared by dispersing 9-AA@Eu-ZIF-8 (50.0 mg) in deionized water (30 mL), followed by addition of 2-thienoyltrifluoroacetone (TTA, 20 mg). The suspension was stirred at room temperature for 20 min. The solid was collected by centrifugation, washed with water and ethanol, and dried to afford 9-AA@Eu-ZIF-8@TTA.

2.4. Sensing experiment

A 1 mM Pi stock solution was prepared using deionized water. For fluorescence measurements, 9-AA@Eu-ZIF-8@TTA (4.0 mg) was dispersed in water (2.0 mL) and sonicated for 5 min to obtain a homogeneous suspension (2 mg mL^{-1}). The suspension was transferred to a 1 cm quartz cuvette, and the Pi stock solution was added stepwise. After mixing and an equilibration time of 0.5 min, fluorescence spectra were recorded from 380 to 700 nm with excitation at 365 nm.

2.5. Determination of Pi in real samples

To evaluate the practical applicability of the Pi sensor, spike-and-recovery experiments were carried out using real water samples, including tap water and lake water. Tap water was collected directly from the laboratory supply, while lake water samples were collected from Baigui Lake (Pingdingshan, Henan Province, China). Prior to analysis, all samples were filtered through 0.22 μm membrane filters before being spiked with Pi standard solutions at different concentrations. Fluorescence measurements were performed in quintuplicate under identical conditions, and the Pi concentrations were quantified using the established calibration curve. The recovery values were calculated to assess the accuracy and reliability of the proposed sensing method.

3. Results and discussion

3.1. Probe design strategy and structural characterization

As illustrated in Scheme 1, the ratiometric fluorescent sensor was constructed through a two-step assembly strategy. In the first step, the blue-emissive dye acridin-9-amine (9-AA) was encapsulated within the pores of an Eu^{3+}-doped ZIF-8 framework to yield 9-AA@Eu-ZIF-8. Subsequently, the antenna ligand 2-thenoyltrifluoroacetone (TTA) was introduced and coordinated to the Eu^{3+} centers, affording the final dual-channel composite, 9-AA@Eu-ZIF-8@TTA. In this design, the physically confined 9-AA serves as a stable and Pi-insensitive internal reference, while the TTA-sensitized Eu^{3+} emission acts as the Pi-responsive channel. Owing to the strong coordination affinity between Pi ions and Eu^{3+} ions, Pi competitively disrupts the Eu^{3+}-TTA coordination, leading to a distinct ratiometric fluorescence response.

The successful synthesis and structural integrity of the materials were confirmed by PXRD, FT-IR spectroscopy, XPS, UV-vis absorption spectroscopy, and TEM-EDS. To verify that the stepwise assembly does not compromise the crystallinity of the host framework, PXRD pattern was first performed. As shown in Fig. 1a, the PXRD pattern of the as-synthesized ZIF-8 agrees well with the simulated pattern, confirming the formation of a highly crystalline framework. Notably, the PXRD patterns of Eu-ZIF-8, 9-AA@Eu-ZIF-8, and 9-AA@Eu-ZIF-8@TTA closely match that of pristine ZIF-8, indicating that Eu^{3+} incorporation, guest encapsulation, and subsequent ligand coordination do not disrupt the host framework structure.

To further elucidate the chemical evolution during the stepwise assembly of the composite, FT-IR spectroscopy was employed (Fig. 1b). The characteristic vibrational bands of the ZIF-8 framework remain well preserved following Eu^{3+} incorporation, confirming the structural integrity of the MOF upon metal doping. Subsequent encapsulation of 9-AA induces no substantial spectral alterations relative to Eu-ZIF-8, indicating that 9-AA is physically encapsulated within the pores without perturbing the framework. Upon postsynthetic coordination with TTA, a new intense absorption band emerges at approximately 1108 cm^{-1}, which can be assigned to the antisymmetric C–F stretching vibration of the CF_3 group in the coordinated TTA ligand. Concomitantly, the original band at ~1172 cm^{-1}, associated with imidazolate ring vibrations of the ZIF-8 framework, undergoes a slight red shift to ~1180 cm^{-1}, likely due to vibrational coupling and local environmental perturbations caused by the nearby Eu-TTA complex. These collective spectral alterations, occurring without disruption to the core ZIF-8 framework bands, provide compelling evidence for the effective coordination of TTA to the Eu^{3+} centers within the composite. Consistently, UV-vis absorption spectroscopy (Fig. 1c) reveals characteristic absorption features corresponding to both 9-AA and TTA in 9-AA@Eu-ZIF-8@TTA, further demonstrating their effective integration within the Eu-ZIF-8 framework.

The elemental composition of the composite was further investigated by XPS analysis. As shown in Fig. 2a, the survey spectrum of 9-AA@Eu-ZIF-8@TTA confirms the presence of Zn, Eu, N, F, and S elements. High-resolution XPS spectra (Fig. 2b–f) display characteristic peaks at 1022.1 eV for Zn 2p, 1135.2 and 1164.7 eV for Eu 3d, 688.4 eV for F 1s, and 164.5 eV for S 2p, respectively, verifying the coexistence of the ZIF-8 framework, Eu^{3+} species, and the coordinated TTA ligand in the final composite.

Finally, the morphology and elemental distribution of the 9-AA@Eu-ZIF-8@TTA composite were systematically investigated by TEM coupled with EDS elemental mapping. As shown in Fig. 3 and Fig. S1, the composite displays a well-defined polyhedral morphology characteristic of pristine ZIF-8, demonstrating that the framework integrity is well preserved throughout the multistep assembly process. The particle size of the composite is estimated to be approximately 300−400 nm (Fig. S2). As shown in Fig. 3b–f, the corresponding EDS elemental maps reveal a homogeneous spatial distribution of Zn, Eu, C, and N, which originate

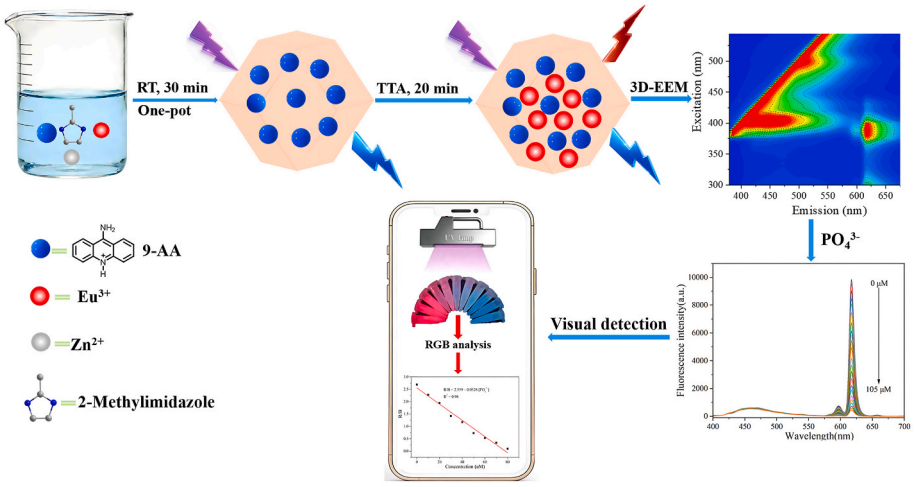

Scheme 1. Fabrication process of 9-AA@Eu-ZIF-8@TTA fluorescent probe and its fluorescence sensing diagram for Pi.

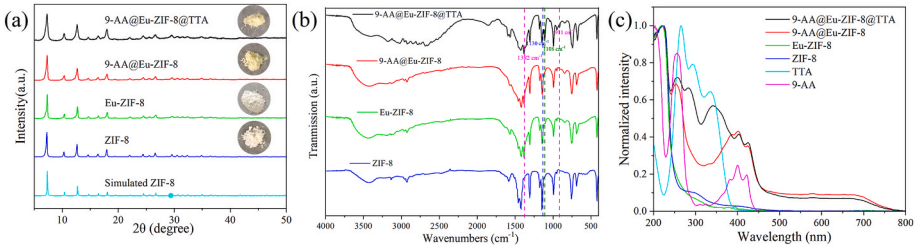

Fig. 1. (a) PXRD patterns of 9-AA@Eu-ZIF-8@TTA, 9-AA@Eu-ZIF-8, Eu-ZIF-8, ZIF-8 and simulated ZIF-8. The photographs of 9-AA@Eu-ZIF-8@TTA, 9-AA@Eu-ZIF-8, Eu-ZIF-8 and ZIF-8 are shown in the inset. (b) FT-IR spectra of 9-AA@Eu-ZIF-8@TTA, 9-AA@Eu-ZIF-8, Eu-ZIF-8 and ZIF-8. (c) UV-vis absorption spectra of 9-AA@Eu-ZIF-8@TTA, 9-AA@Eu-ZIF-8, Eu-ZIF-8, ZIF-8, 9-AA and TTA.

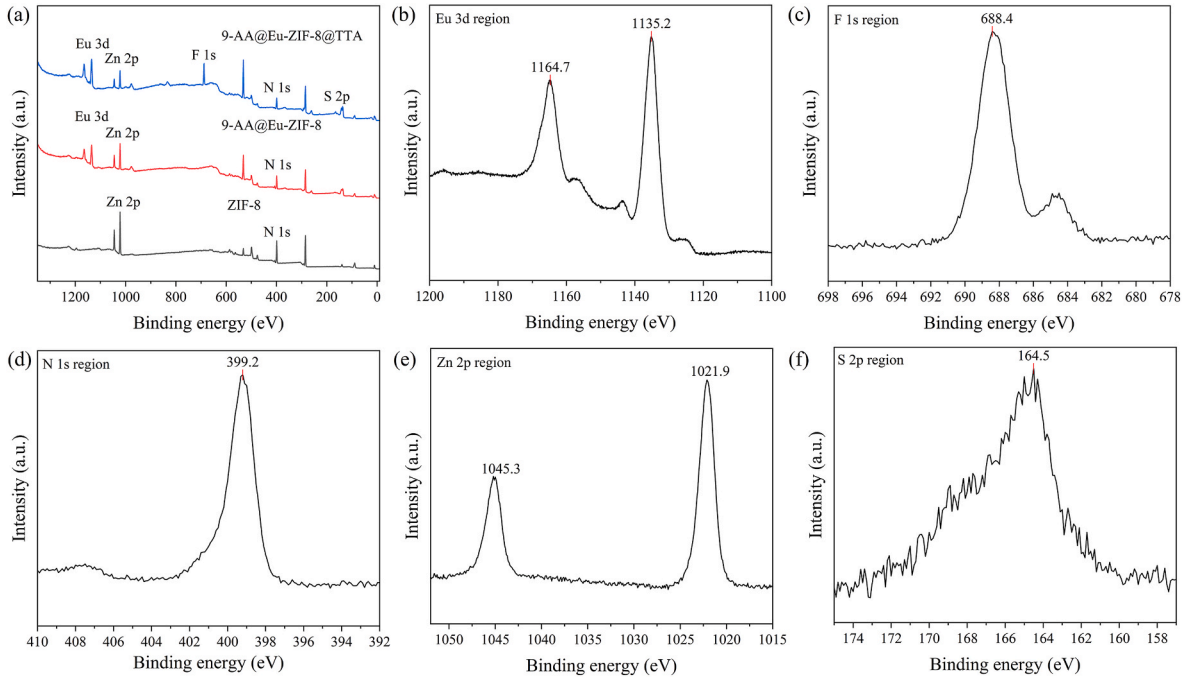

Fig. 2. Full XPS spectra of 9-AA@Eu-ZIF-8@TTA, 9-AA@Eu-ZIF-8 and ZIF-8 (a); Eu 3d (b), F 1s (c), N 1s (d), Zn 2p (e) and S 2p region of 9-AA@Eu-ZIF-8@TTA.

from the ZIF-8 framework and coordinated organic ligands. In addition, the presence of F and S elements, characteristic of the TTA antenna ligand, is clearly observed and uniformly distributed throughout the particles. The high degree of spatial overlap among these elemental signals provides compelling evidence for the successful and homogeneous incorporation of Eu^{3+} ions together with the coordinated TTA

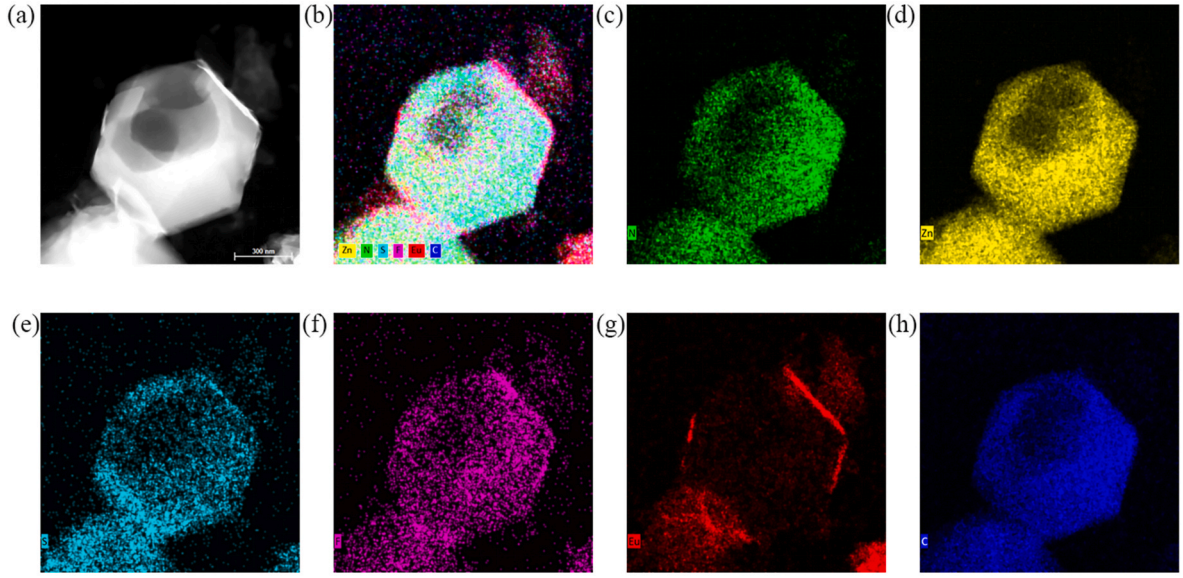

Fig. 3. The TEM images (a, b) and EDS mapping images (c-h) of 9-AA@Eu-ZIF-8@TTA.

ligand within the ZIF-8 host matrix.

3.2. Photoluminescence analysis

The photoluminescence properties of 9-AA, 9-AA@Eu-ZIF-8, Eu-ZIF-8@TTA, and 9-AA@Eu-ZIF-8@TTA were systematically examined by three-dimensional excitation−emission matrix (3D-EEM) fluorescence spectroscopy (Fig. 4). As shown in Fig. 4a, two well-resolved emission bands centered at 469 and 617 nm are observed, corresponding to the blue emission of 9-AA and the characteristic red emission of Eu^{3+}

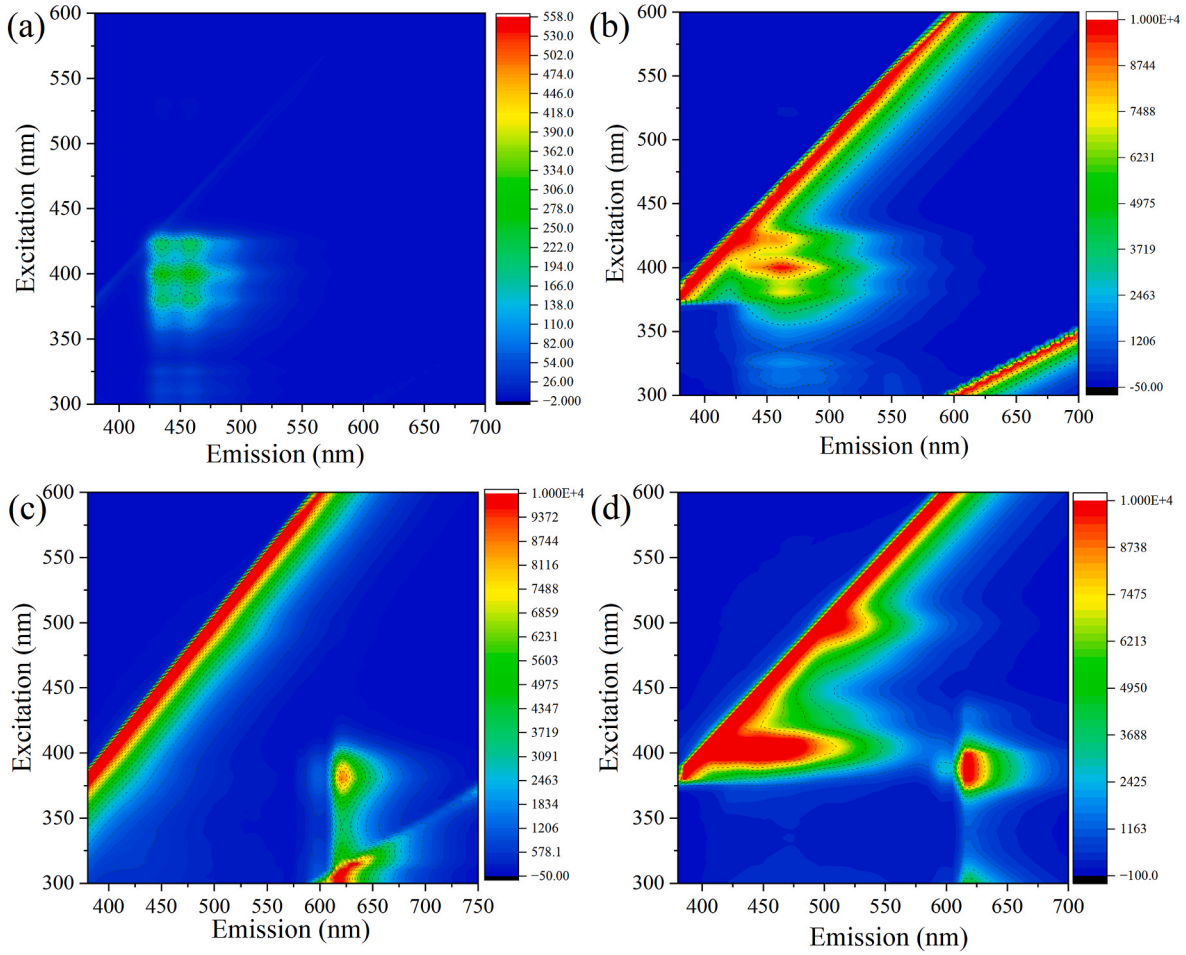

Fig. 4. 3D-EEM spectra of 9-AA solution (a), 9-AA@Eu-ZIF-8 (b), Eu-ZIF-8@TTA (c) and 9-AA@Eu-ZIF-8@TTA (d) powders.

(Fig. 4b and c), respectively, thereby confirming the coexistence of both luminophores within the composite.

To gain deeper insight into the excitation–emission behavior, the luminescence characteristics of the as-synthesized materials were further investigated using conventional two-dimensional excitation and emission spectroscopy (Fig. S3). Upon excitation at 365 nm, 9-AA@Eu-ZIF-8 displays a single intense blue emission band centered at 460 nm, originating from the encapsulated 9-AA molecules. Following coordination of the antenna ligand TTA, the resulting 9-AA@Eu-ZIF-8@TTA exhibits a sharp red emission peak at 617 nm, corresponding to the $^5D_0 \rightarrow {}^7F_2$ transition of Eu^{3+}. The coexistence of these two spectrally distinct emission channels provides a solid basis for ratiometric fluorescence sensing. Furthermore, excitation spectra recorded at the blue emission of 9-AA and the red emission of Eu^{3+} demonstrate that both luminophores can be efficiently excited at a single wavelength of 365 nm. Given the widespread availability of 365 nm UV lamps for visual inspection, the Pi-induced color change of the probe suspension can be directly correlated with its fluorescence spectroscopic response. Accordingly, 365 nm was selected as the excitation wavelength for all subsequent sensing experiments.

To further corroborate the spectroscopic findings and evaluate the visual fluorescence response, the luminescence behavior of the powder samples under 365 nm ultraviolet (UV) excitation was systematically evaluated (Fig. S4). Under UV illumination, pristine 9-AA and Eu-ZIF-8@TTA exhibit no detectable visible emission. In contrast, the composite samples display distinct fluorescence responses, with 9-AA@Eu-ZIF-8 emitting blue light and Eu-ZIF-8@TTA exhibiting red emission. Notably, 9-AA@Eu-ZIF-8@TTA produces intense orange-red luminescence, indicating the successful co-integration of 9-AA, Eu^{3+}, and the antenna ligand TTA within a single framework, along with efficient energy transfer among the constituent components.

3.3. Fluorescence titration of Pi

Based on the well-defined dual-emission behavior and single-wavelength excitation capability discussed above, the Pi sensing performance of 9-AA@Eu-ZIF-8@TTA was systematically evaluated. As shown in Fig. 5, increasing the Pi concentration from 0 to 105 μM results in pronounced changes in the fluorescence spectra, where the Eu^{3+}-centered emission at 617 nm decreases progressively, while the 9-AA emission at 460 nm remains essentially unchanged. This well-resolved dual-emission behavior enables reliable ratiometric quantification of Pi.

To establish suitable sensing conditions, the response kinetics and pH tolerance of the probe were evaluated. As illustrated in Fig. 5a, the ratiometric signal (I_{617}/I_{460}) reaches a steady state within 0.5 min after Pi addition (Fig. S5), indicating a rapid response. The probe also maintains stable ratiometric performance over a broad pH range of 3–11 (Fig. S6). Accordingly, a reaction time of 0.5 min at neutral pH was selected for subsequent measurements.

Under these optimized conditions, the ratiometric signal (I_{617}/I_{460}) decreases monotonically with increasing Pi concentration, whereas the reference emission at 460 nm remains nearly constant (Fig. 5a). A good linear relationship ($R^2 = 0.992$) is obtained between I_{617}/I_{460} and Pi concentration over the range of 0–80.0 μM (Fig. 5c). The limit of

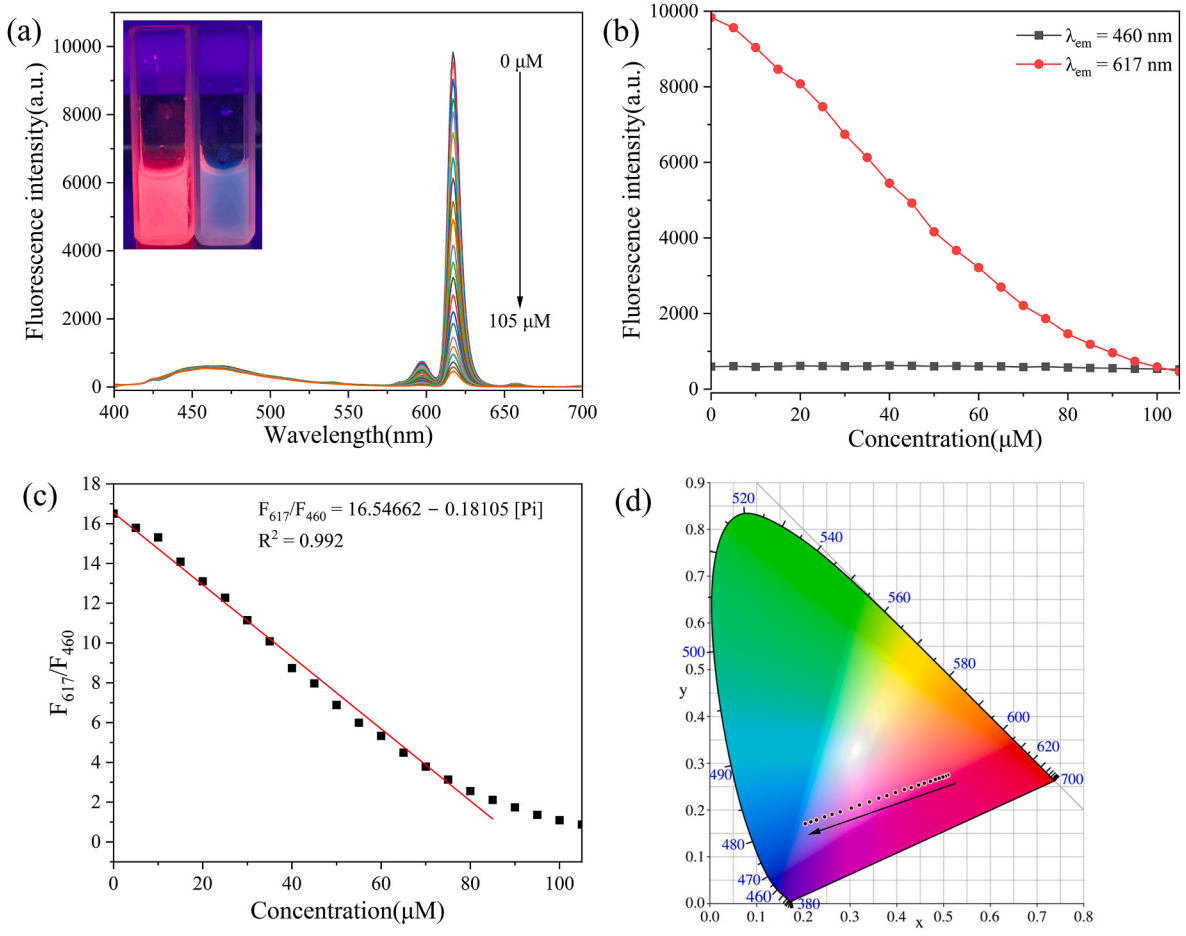

Fig. 5. (a) Fluorescence emission spectra of 9-AA@Eu-ZIF-8@TTA composite in the presence of different Pi concentrations. Inset: the photographs before and after the addition of 105.0 μM Pi. (b) The response of fluorescence intensity of 9-AA@Eu-ZIF-8@TTA composite at 460 nm and 617 nm to different concentrations of Pi. (c) The linear relationship between F_{617}/F_{460} and the concentration of Pi. (d) The corresponding change of CIE chromaticity coordinates calculated from the emission spectra.

detection (LOD), calculated to be 0.48 μM based on 3σ/k, is well below the Pi thresholds specified in environmental protection guidelines. As summarized in Table 1, although the detection limit of 9-AA@Eu-ZIF-8@TTA is not the lowest among reported MOF-based probes, it uniquely integrates a dual-emission ratiometric response, a competitive coordination mechanism, rapid response (0.5 min), wide pH tolerance, and direct visual readout under UV illumination.

In addition to spectroscopic quantification, the probe exhibits a distinct fluorescence color transition from red to blue under 365 nm UV illumination as the Pi concentration increases (Fig. 6a), consistent with the ratiometric fluorescence response. This visual change is accompanied by a corresponding shift in the CIE chromaticity coordinates from (0.4390, 0.2774) to (0.2262, 0.1623) (Fig. 5d). To enable semi-quantitative analysis, the fluorescence images were further processed using a smartphone-based color analysis application to extract the red (R) and blue (B) channel intensities. As shown in Fig. 6a, the R/B ratio decreases monotonically with increasing Pi concentration and exhibits a good linear relationship described by $R/B = 2.559 - 0.0328$ [Pi] ($R^2 = 0.98$), demonstrating that the visual fluorescence response can be converted into a quantitative colorimetric parameter for on-site and instrument-free semi-quantitative Pi detection.

Beyond sensitivity and visual readability, the photostability is a critical parameter for practical applications. Therefore, the ratiometric fluorescence response of 9-AA@Eu-ZIF-8@TTA was monitored over seven consecutive days under identical conditions. As shown in Fig. S7, the fluorescence intensity ratio (I_{617}/I_{460}) remains nearly constant throughout the testing period, with only negligible fluctuations observed. This excellent signal stability indicates that the probe maintains its structural integrity and sensing performance over time, thereby supporting its suitability for long-term storage and repeated use in practical Pi monitoring applications.

3.4. Selectivity assessment

The selectivity and anti-interference capability of the 9-AA@Eu-ZIF-8@TTA probe toward phosphate (Pi) were systematically evaluated in the presence of various potential interfering species. As illustrated in Fig. 6b, a series of common ions, including Zn^{2+}, Ni^{2+}, K^+, Na^+, Mg^{2+}, Cu^{2+}, Co^{2+}, Al^{3+}, Fe^{3+}, HCO_3^-, SO_4^{2-}, CO_3^{2-}, NO_3^-, Br^-, I^-, S^{2-}, and citrate, exerted no obvious interference on the determination of Pi. For Pi analogs, such as PO_3^{2-}, $P_2O_7^{4-}$, trimethyl phosphate (TMP) and dimethyl methylphosphonate (DMMP), negligible interference was also observed except for pyrophosphate. Nevertheless, pyrophosphate is rarely present in biological and environmental samples [42], which confirms that the proposed method possesses excellent selectivity for Pi. The high specificity of this ratiometric probe toward Pi can be attributed to the stronger affinity of tetrahedrally coordinated Pi with Eu^{3+} compared to other spherical or linear ions [49]. Notably, this observation is consistent with previous reports [42], which have demonstrated that pyrophosphate is the primary interfering phosphorus-containing species in Eu-based Pi sensing systems. Obviously, these results clearly show that the ratiometric fluorescent probe has good anti-interference ability and is well-suited for Pi detection in real water samples.

Table 1
Comparison with some MOFs-based fluorescent probes for Pi detecting.

Materials	Type of probe	Response time (min)	LOD (μM)	Linear range (μM)	Ref
CDs/Zn-TCPP (BPDC)	Ratiometric	9	0.13	0–131.25	[44]
CDs/AuNCs@ZIF-8	Ratiometric	10	0.27	1–120	[45]
Ru@UiO-66-NH_2	Ratiometric	5	0.029	0.1–12, 12–20	[32]
Zr-PDI	Turn-on	60	0.023	2–60	[33]
PMOF@Al_2O_3	Turn-on	10	0.16	0–180	[34]
Tb-BTC	Turn-off	40	2.97	5–90	[35]
GCDs/Eu-BDC	Ratiometric	4	0.070	0–10, 10–45	[3]
UiO-66(Fe/Zr)–NH_2	Ratiometric	35	0.085	0.2–266.7	[46]
Tb/Eu-MOF	Ratiometric	2	0.084	0–6.0	[36]
Eu/Ce/UiO-66-$(COOH)_2$	Ratiometric	1	0.247	0.3–20	[47]
RhB@UiO-66-NH_2	Ratiometric	120	2.0	80–400	[48]
UiO-66-NH_2/Eu^{3+}@MOF-808	Ratiometric	10	0.087	1–200	[40]
COF-MOF	Ratiometric	10	0.95	5–100	[43]
9-AA@Eu-ZIF-8@TTA	Ratiometric	0.5	0.48	0–80	This work

3.5. Application

To evaluate the practical applicability of the 9-AA@Eu-ZIF-8@TTA probe, spike-and-recovery experiments were carried out using tap water and lake water samples containing different concentrations of Pi. Concurrently, the concentrations of Pi were quantified via the standard phosphomolybdenum blue spectrophotometry to validate the analytical accuracy of the proposed approach. Each measurement was performed in quintuplicate, and the results are summarized in Table 2. The determined Pi concentrations agree well with the spiked values and the standard method, affording satisfactory recoveries in the range of 97.0−103.2% with low relative standard deviations (RSD <3.92%). These results clearly demonstrate the accuracy, reliability, and practical feasibility of the proposed probe for Pi detection in complex environmental water matrices.

3.6. Mechanism

To elucidate the sensing mechanism, a series of control experiments, including PXRD, FT-IR, XPS, TEM-EDS and fluorescence lifetime analyses, were systematically conducted after exposure of the probe to excess Pi. As shown in Fig. 7a, the PXRD pattern of 9-AA@Eu-ZIF-8@TTA remains identical to that of the pristine material after Pi treatment, indicating that the ZIF-8 framework retains its crystallinity and that structural collapse is not responsible for the observed fluorescence changes.

Given that no structural degradation was observed, FT-IR spectroscopy was subsequently employed to probe changes in the coordination environment. Upon the addition of Pi, noticeable changes are observed in the spectral region related to the Eu^{3+} coordination environment. In particular, the vibrational features associated with the Eu^{3+}–TTA complex are significantly attenuated, indicating partial or complete dissociation of the TTA antenna ligand from the Eu^{3+} centers. Meanwhile, two new absorption bands emerge at around 1070 and 588 cm^{-1}, which can be assigned to the P–O stretching and bending vibrations of Pi species coordinated to Eu^{3+}, respectively. Notably, the characteristic bands of the ZIF-8 framework remain essentially unchanged after Pi addition, suggesting that the competitive coordination process occurs preferentially at the Eu^{3+} sites without disrupting the MOF structure. These FT-IR results provide direct spectroscopic evidence for the Pi-induced coordination substitution mechanism responsible for the selective quenching of Eu^{3+} emission.

XPS analysis further provides elemental-level evidence supporting the proposed mechanism. As shown in Fig. 7c, Pi treatment leads to the disappearance of the F 1s and S 2p signals associated with the TTA ligand. In contrast, the persistence of the Zn 2p, C 1s, N 1s, and Eu 3d peaks confirms that the overall framework composition remains intact. These observations indicate that Pi ions preferentially coordinate to Eu^{3+} centers, displacing the TTA ligand and thereby disrupting the antenna effect responsible for Eu^{3+}-centered emission.

To provide spatially resolved confirmation of the proposed mechanism, TEM-EDS elemental mapping was performed after Pi treatment. As

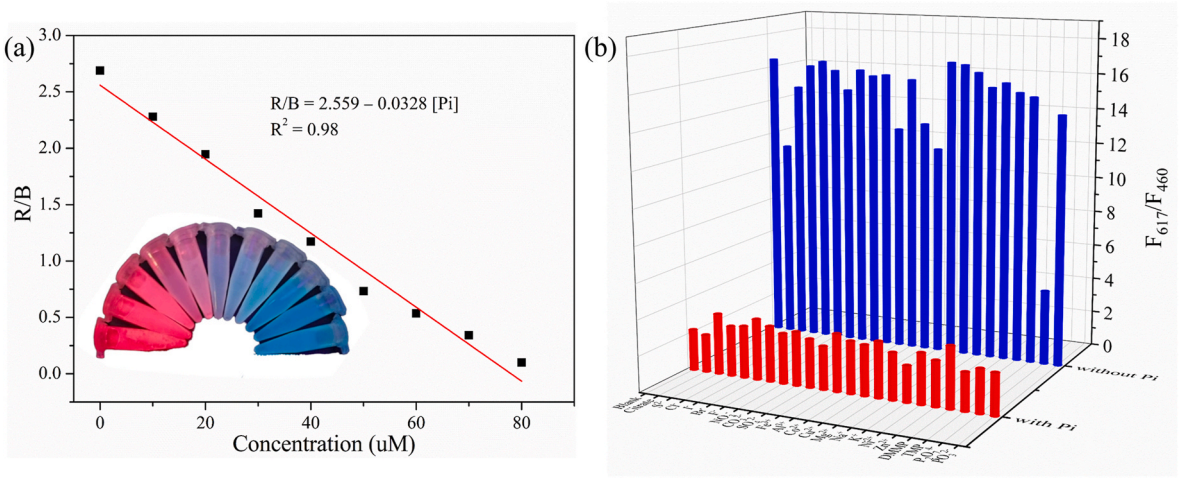

Fig. 6. (a) Linear plot of color change (R/B) of 9-AA@Eu-ZIF-8@TTA suspension solution vs. Pi concentration; the inset shows the photographs irradiated with a UV lamp at 365 nm. (b) Fluorescence responses of 9-AA@Eu-ZIF-8@TTA composite to Pi (80.0 μM) and various interferents 80.0 μM). (For interpretation of the references to color in this figure legend, the reader is referred to the Web version of this article.)

Table 2
Detection of Pi in real samples (n = 5).

Samples	Spiked (μM)	PBS[a] (μM)[b]	This work (μM)[a]	Recoveries (%)	RSD (%)
Tap water	0	N.D[c]	N.D[c]	–	–
	20.0	19.7	20.3	101.5	3.82
	40.0	40.8	39.3	98.2	2.74
	60.0	59.7	61.4	102.3	4.13
Lake water	0	N.D	N.D	–	–
	20.0	19.6	19.4	97.0	4.27
	40.0	40.3	41.3	103.2	3.92
	60.0	59.7	58.9	98.2	1.95

[a] Phosphomolybdenum blue spectrophotometry.
[b] Mean.
[c] Not detected.

shown in Fig. 8, the composite maintains its characteristic morphology, while the uniform distribution of Zn, N, and C further confirms the structural stability of the ZIF-8 framework. Importantly, a distinct P signal is detected, and its spatial overlap with Eu indicates direct coordination of Pi to the Eu^{3+} sites. Taken together, the combined spectroscopic and microscopic results consistently support a competitive coordination mechanism, in which Pi binds strongly to Eu^{3+}, displacing the sensitizing TTA ligand and ultimately leading to quenching of the Eu^{3+}-centered red emission.

To clarify the sensing mechanism for Pi, we carried out time-resolved fluorescence measurements on both emission channels of 9-AA@Eu-ZIF-8@TTA over a range of Pi concentrations. The blue band at 460 nm arises from the encapsulated 9-AA fluorophore, whereas the red band at 617 nm is associated with Eu^{3+}-centered emission. Because these two signals originate from distinct emissive species, their absolute lifetimes are not directly comparable. However, the more relevant question is whether either decay pathway is perturbed upon Pi addition. As shown in Fig. 9, the decay traces for both channels remain essentially unchanged in the presence of Pi. Importantly, to further confirm that the 9-AA reference signal is intrinsically insensitive to Pi, control experiments were performed on 9-AA@ZIF-8 (i.e., without Eu^{3+} or TTA). The fluorescence lifetime of 9-AA in this control system also showed no detectable change upon Pi addition (shown in Fig. S8), confirming that the photophysical properties of the encapsulated 9-AA are not affected by Pi under the experimental conditions. More importantly, although the Eu^{3+} emission intensity is markedly reduced in the steady-state spectra, its lifetime shows no appreciable variation. This observation argues against a dynamic quenching pathway as the dominant mechanism and instead points to a static quenching process associated with coordination changes in the local Eu^{3+} environment. Considered together with the PXRD, FT-IR, XPS, and TEM-EDS results, these observations support a competitive coordination mechanism: Pi preferentially binds to Eu^{3+} centers and displaces coordinated TTA ligands, thereby disrupting ligand-to-metal energy transfer and decreasing the population of emissive Eu^{3+}-TTA sites. The net effect is a pronounced loss of Eu^{3+}-centered emission intensity without a measurable change in the decay behavior of the remaining emissive centers.

4. Conclusion

In summary, a self-calibrating dual-emissive MOF-based fluorescent probe, 9-AA@Eu-ZIF-8@TTA, has been developed for the sensitive and selective detection of Pi. By spatially integrating a photostable internal reference (9-AA) and a Pi-responsive Eu^{3+}-centered emission within a

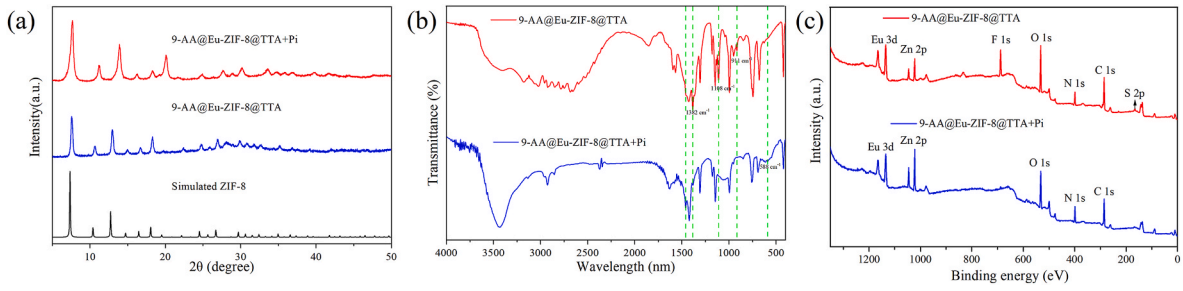

Fig. 7. (a) PXRD spectra of 9-AA@Eu-ZIF-8@TTA before and after the addition of excess Pi. (b) FT-IR spectra of 9-AA@Eu-ZIF-8@TTA before and after the addition of excess Pi. (c) XPS spectra of 9-AA@Eu-ZIF-8@TTA before and after the addition of excess Pi.

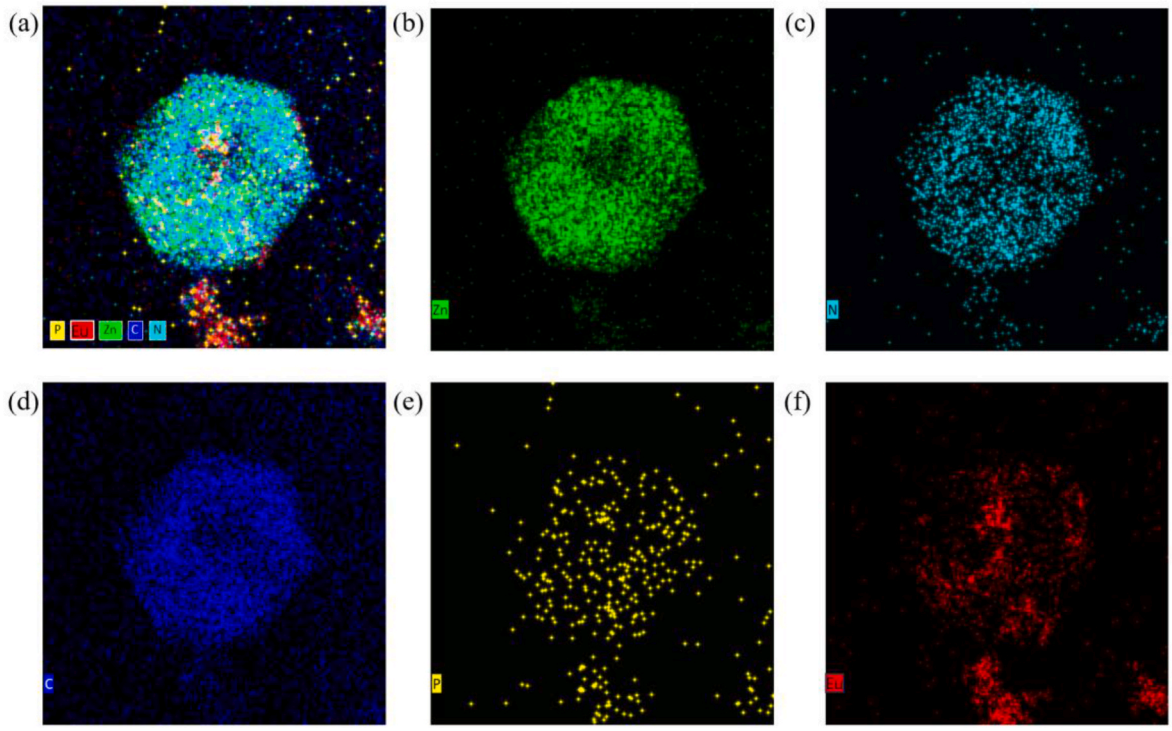

Fig. 8. The TEM and EDS mapping images of 9-AA@Eu-ZIF-8@TTA after the addition of excess Pi.

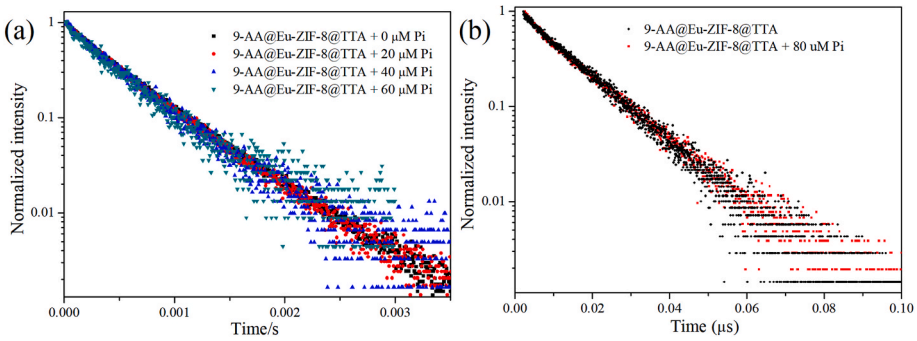

Fig. 9. Fluorescence decay (λ_{em} = 617 nm) (a) and (λ_{em} = 460 nm) curves of 9-AA@Eu-ZIF-8@TTA ratiometric probe after adding different concentrations of Pi.

ZIF-8 framework, the probe enables reliable ratiometric fluorescence sensing with a linear response over the range of 0–80 μM and a detection limit of 0.48 μM. The sensing performance is further underscored by rapid response kinetics, broad pH tolerance, and excellent selectivity against competing species. Importantly, the probe allows direct visual readout under UV illumination and enables semi-quantitative analysis through smartphone-based RGB evaluation, highlighting its potential for instrument-free on-site detection. Mechanistic investigations reveal that Pi selectively coordinates to the Eu^{3+} centers, displacing the sensitizing TTA ligand and suppressing Eu^{3+} emission through a competitive coordination process. Beyond Pi detection, this work establishes a general and versatile design strategy for constructing robust ratiometric sensing platforms by integrating host–guest encapsulation with analyte-triggered coordination chemistry in MOF systems.

CRediT authorship contribution statement

Jinfeng Zhou: Conceptualization, Data curation, Formal analysis, Funding acquisition, Investigation, Methodology, Supervision, Writing – review & editing. **Hailin Qiu:** Conceptualization, Formal analysis, Investigation, Writing – original draft. **Qing Zhou:** Investigation, Methodology, Resources. **Chunjie Chu:** Conceptualization, Investigation, Methodology, Supervision. **Xiaodong Zhang:** Data curation, Investigation. **Yanhong Xu:** Data curation, Investigation, Methodology.

Declaration of competing interest

The authors declare that they have no known competing financial interests or personal relationships that could have appeared to influence the work reported in this paper.

Acknowledgment

This work was funded by the Basic Research Program of Key Scientific Research Projects in Higher Education Institutions in Henan Province (23B150009) and Henan Provincial Science and Technology Research Project (262102320116).

Appendix A. Supplementary data

Supplementary data to this article can be found online at https://doi.org/10.1016/j.aca.2026.345572.

Data availability

Data will be made available on request.

References

[1] V.C. Pierre, R.K. Wilharm, Design principles and applications of selective lanthanide-based receptors for inorganic phosphate, Front. Chem. 10 (2022) 821020.

[2] M.V. Ramakrishnam Raju, S.M. Harris, V.C. Pierre, Design and applications of metal-based molecular receptors and probes for inorganic phosphate, Chem. Soc. Rev. 49 (2020) 1090–1108.

[3] Y. Li, R. Zhou, L. Zhang, N. Bi, J. Gou, J. Wu, L. Jia, J. Xu, Integration of Eu-based metal−organic frameworks and carbon dots for multicolor visual intelligent detection of phosphate, Talanta 284 (2025) 127270.

[4] D.J. Conley, H.W. Paerl, R.W. Howarth, D.F. Boesch, S.P. Seitzinger, K.E. Havens, C. Lancelot, G.E. Likens, Ecology controlling eutrophication: nitrogen and phosphorus, Science 323 (2009) 1014–1015.

[5] M. Lürling, F. van Oosterhout, Controlling eutrophication by combined bloom precipitation and sediment phosphorus inactivation, Water Res. 47 (2013) 6527–6537.

[6] T.M. Leclercq, S.M. Pitson, Cellular signalling by sphingosine kinase and sphingosine 1-phosphate, IUBMB Life 58 (2006) 467–472.

[7] L. Szyc, M. Yang, T. Elsaesser, Ultrafast energy exchange via water-phosphate interactions in hydrated DNA, J. Phys. Chem. B 114 (2010) 7951–7957.

[8] S. Chande, C. Bergwitz, Role of phosphate sensing in bone and mineral metabolism, Nat. Rev. Endocrinol. 14 (2018) 637–655.

[9] F. Albaaj, A.J. Hutchison, Hyperphosphataemia in renal failure, Drugs 63 (2003) 577–596.

[10] E.W. Young, J.M. Albert, S. Satayathum, D.A. Goodkin, R.L. Pisoni, T. Akiba, T. Akizawa, K. Kurokawa, J. Bommer, L. Piera, F.K. Port, Predictors and consequences of altered mineral metabolism: the dialysis outcomes and practice patterns study, Kidney Int. 67 (2005) 1179–1187.

[11] J. Xu, H. Zhang, W. Zhang, P. Li, W. Zhang, H. Wang, B. Tang, Fluorescent nanosensor for in situ detection of phosphate and alkaline phosphatase in mice with parathyroid dysfunction, Chem. Commun. 56 (2020) 2431–2434.

[12] C. Forano, H. Farhat, C. Mousty, Recent trends in electrochemical detection of phosphate in actual waters, Curr. Opin. Electrochem. 11 (2018) 55–61.

[13] M.S. Han, D.H. Kim, Naked-eye detection of phosphate ions in water at physiological pH: a remarkably selective and easy-to-assemble colorimetric phosphate-sensing probe, Angew. Chem. Int. Ed. 41 (2002) 3809–3811.

[14] X. Li, X. Niu, P. Liu, X. Xu, D. Du, Y. Lin, High-performance dual-channel ratiometric colorimetric sensing of phosphate ion based on target-induced differential oxidase-like activity changes of Ce−Zr bimetal−organic frameworks, Sens. Actuators B Chem. 321 (2020) 128546.

[15] X. Li, B. Liu, K. Ye, L. Ni, X. Xu, F. Qiu, J. Pan, X. Niu, Highly sensitive and specific colorimetric detection of phosphate using Zr(IV) to synergistically suppress the peroxidase-mimicking activity of hydrophilic Fe_3O_4 nanocubes, Sens. Actuators B Chem. 297 (2019) 126822.

[16] X. Li, B. Liu, Z. Hu, P. Liu, K. Ye, J. Pan, X. Niu, Smartphone-assisted off–on photometric determination of phosphate ion based on target-promoted peroxidase-mimetic activity of porous $Ce_xZr_1-xO_2$ nanocomposites, Environ. Res. 189 (2020) 109921.

[17] J. He, H. Sun, J. Dai, H. Wang, L. Yu, W. Zhou, Z. Shao, In situ growth of nanoflake and nanoflower-like Ni hydrated hydroxide on Ni foam as a free-standing electrode for high-performance phosphate detection, J. Hazard. Mater. 392 (2020) 122313.

[18] U. Sivasankaran, L. Reinke, S.K. Anand, K. Malecka, K.G. Kumar, H. Radecka, S. Kubik, J. Radecki, Ultrasensitive electrochemical sensing of phosphate in water mediated by a dipicolylamine−zinc(II) complex, Sens. Actuators B Chem. 321 (2020) 128474.

[19] S. Sun, Q. Chen, S. Sheth, G. Ran, Q. Song, Direct electrochemical sensing of phosphate in aqueous solutions based on phase transition of calcium phosphate, ACS Sens. 5 (2020) 541–548.

[20] S.N. Li, Y. You, W.G. Hu, G.J. Gao, X.Y. Jiang, J.G. Yu, A sensitive single-layer graphene oxide-based sensor for electrochemical sensing of phosphate anion, Process Saf. Environ. Prot. 178 (2023) 786–794.

[21] Y. Li, R. Zhou, F. Xue, N. Bi, L. Zhang, Q. Li, K. Shi, J. Wu, L. Jia, J. Xu, Ratiometric fluorescent nanoprobes based on lanthanide coordination polymers for visual intelligent detection of phosphate, Chem. Eng. J. 515 (2025) 163463.

[22] X. Wang, G. Chen, Y. Yu, L. Meng, F. Lin, W. He, J. Chen, D. Zhou, F. Zhu, A novel Lu(III)-based rare-earth metal−organic framework for rapid detection of phosphate with triple-signal output, Food Chem. 499 (2026) 147371.

[23] B. Teixeira, R. Mendes, Analysis of added phosphates in hake fillets by ion-exchange chromatography: a case study of false positives induced by nucleotides coelution, Food Chem. 368 (2022) 130841.

[24] C. Chang, Introduction: fluorescent probes in biology, Chem. Rev. 124 (2024) 11639–11640.

[25] S. Xu, K.C. Yan, Z.H. Xu, Y. Wang, T.D. James, Fluorescent probes for targeting the Golgi apparatus: design strategies and applications, Chem. Soc. Rev. 53 (2024) 7590–7631.

[26] X. Xu, M.Y. Ma, T. Sun, X. Zhao, L. Zhang, Luminescent guests encapsulated in metal−organic frameworks for portable fluorescence sensor and visual detection applications: a review, Biosens. Bioelectron. 134 (2023) 435.

[27] M. Brady, V.I. Shchepetkina, I. González-Recio, M.L. Martínez-Chantar, D. Buccella, Ratiometric fluorescent sensors illuminate cellular magnesium imbalance in a model of acetaminophen-induced liver injury, J. Am. Chem. Soc. 145 (2023) 21841–21850.

[28] S.H. Park, N. Kwon, J.H. Lee, J. Yoon, I. Shin, Synthetic ratiometric fluorescent probes for detection of ions, Chem. Soc. Rev. 49 (2020) 143–179.

[29] S. Wu, H. Min, W. Shi, P. Cheng, Multicenter metal–organic framework-based ratiometric fluorescent sensors, Adv. Mater. 32 (2020) 1805871.

[30] R. Jia, W. Tian, H. Bai, J. Zhang, S. Wang, J. Zhang, Amine-responsive cellulose-based ratiometric fluorescent materials for real-time and visual detection of shrimp and crab freshness, Nat. Commun. 10 (2019) 795.

[31] S. Wu, L. Sun, Y. Bian, F. Wu, D. Shi, H. Xu, A ratiometric turn-on fluorescent probe for the detection of BF_3 based on imidazole-quinoline, Spectrochim. Acta Mol. Biomol. Spectrosc. 332 (2025) 125748.

[32] Q. Wang, C. Wang, L. Xie, H. Yu, Y. Wang, X.E. Zhao, S.Y. Zhu, R.J. Wang, Dual-emissive Ru@UiO-66-NH_2 composite for selective visual detection of phosphate and arsenate, Anal. Chim. Acta 1378 (2025) 344704.

[33] C. Yang, S. Tian, Y. Zhao, L. Yang, L. Mo, W. Lin, A unique fluorescence metal–organic framework for ultrasensitive fluorescent and colorimetric bimodal detection of phosphate, Spectrochim. Acta Mol. Biomol. Spectrosc. 329 (2025) 125571.

[34] G. Zhang, Y. Ma, H. Chai, K. Yu, Y. Li, S. Wang, J. Ma, L. Qu, W. Tan, X. Zhang, Porphyrinic metal−organic framework@alumina nanocomposite fluorescent probe: two-stage stimuli-responsive behavior and phosphate sensing, Sens. Actuators B Chem. 370 (2022) 132395.

[35] S. Ding, X. Wang, Terbium-based metal–organic framework and its immobilized nanofibrous membrane for selective detection and efficient removal of phosphate, Chem. Eng. J. 464 (2023) 142751.

[36] J.R. Zhao, J. Zhang, W.X. Yang, H. Wang, N. Zhang, Y.Z. Fang, Q. Ke, Rational design of core-shell Ln-MOF hierarchitecture for ratiometric fluorescent sensing and bioimaging of phosphate or ATP, Sens. Actuators B Chem. 389 (2023) 133907.

[37] C. Jia, T. He, G.M. Wang, Zirconium-based metal–organic frameworks for fluorescent sensing, Coord. Chem. Rev. 476 (2023) 214930.

[38] F. Xue, X. Yang, R. Mou, R. Huang, L. Jiang, L. He, J. Li, Y. Deng, H. Wang, Y. He, Cerium-based metal–organic frameworks mediated dual-mode sensor for accurate quantification of pyrophosphate in aqueous media, Sens. Actuators B Chem. 442 (2025) 138165.

[39] S. Bhowal, S. Mondal, Recent advances in fluorescent metal–organic framework-based detection of heavy metal contaminants in water, Talanta 300 (2026) 129233.

[40] K. Yi, X. Zhang, L. Zhang, Smartphone-based ratiometric fluorescent definable system for phosphate by merged metal-organic frameworks, Sci. Total Environ. 772 (2021) 144952.

[41] Q. Peng, C. Qiu, P. Huang, F.Y. Wu, An integrated ratiometric fluorescent probe based on MOF-on-MOF heterostructure for sensitive detection of nerve agent simulants, Talanta 296 (2026) 128528.

[42] G. Li, C. Tong, Dual-functional lanthanide metal–organic frameworks for visual and ultrasensitive ratiometric fluorescent detection of phosphate based on aggregation-induced energy transfer, Anal. Chim. Acta 1133 (2020) 11–19.

[43] Y.J. Yu, W. Li, S.B. Ren, X.J. Zhou, D.M. Han, Rational design of COF–MOF composites for ratiometric fluorescence detection of phosphate, New J. Chem. 47 (2023) 6186–6190.

[44] Y. Zhang, B. Ren, W. Dong, Q. Duan, T. Fei, A ratiometric fluorescence probe based on porphyrin-based MOF for phosphate ions detection, Microchem. J. 211 (2025) 113156.

[45] J. Liu, Y. Liu, W. Wang, S. Zhang, L. Tang, P. Ma, D. Song, Q. Fei, A ratiometric fluorescent sensor for the detection of phosphate, Luminescence 38 (2023) 152–158.

[46] X. Li, P. Liu, X. Niu, K. Ye, L. Ni, D. Du, J. Pan, Y. Lin, Tri-functional Fe-Zr bi-metal-organic frameworks enable high-performance phosphate ion ratiometric fluorescent detection, Nanoscale 12 (2020) 19383–19389.

[47] C. Gong, Z. Li, G. Liu, S. Pu, Ratiometric fluorescent sensing for phosphate based on Eu/Ce/UiO-66-$(COOH)_2$ nanoprobe, Spectrochim. Acta 252 (2021) 119493.

[48] N. Gao, J. Huang, L. Wang, J. Feng, P. Huang, F. Wu, Ratiometric fluorescence detection of phosphate in human serum with a metal-organic frameworks-based nanocomposite and its immobilized agarose hydrogels, Appl. Surf. Sci. 459 (2018) 686–692.

[49] K.S. Asha, R. Bhattacharjee, S. Mandal, Complete transmetalation in a metalorganic framework by metal ion metathesis in a single crystal for selective sensing of phosphate ions in aqueous media, Angew. Chem. Int. Ed. 55 (2016) 11528–11532.